BBA - Bioenergetics 1860 (2019) 402–413

Contents lists available at ScienceDirect

BBA - Bioenergetics

journal homepage: www.elsevier.com/locate/bbabio

Tuning the redox properties of a [4Fe-4S] center to modulate the activity of Mo-*bis*PGD periplasmic nitrate reductase

Kamal Zeamari[a], Guillaume Gerbaud[a], Sandrine Grosse[b], Vincent Fourmond[a], Florence Chaspoul[c], Frédéric Biaso[a], Pascal Arnoux[b], Monique Sabaty[b], David Pignol[b], Bruno Guigliarelli[a], Bénédicte Burlat[a,*]

[a] Aix Marseille Univ, CNRS, BIP Laboratoire de Bioénergétique et Ingénierie des Protéines, Marseille, France
[b] Aix Marseille Univ, CEA, CNRS, BIAM Institut de Biosciences et Biotechnologies, Saint Paul-Lez-Durance, France
[c] Aix Marseille Univ, Avignon Université, CNRS, IRD, IMBE Institut Méditerranéen de Biodiversité et d'Ecologie Marine et continentale, Marseille, France

ARTICLE INFO

Keywords:
Molybdenum-containing enzymes
Nitrate reductase
Biological electron transfer
Site-directed mutagenesis
EPR spectroscopy

ABSTRACT

Molybdoenzymes are ubiquitous in living organisms and catalyze, for most of them, oxidation-reduction reactions using a large range of substrates. Periplasmic nitrate reductase (NapAB) from *Rhodobacter sphaeroides* catalyzes the 2-electron reduction of nitrate into nitrite. Its active site is a Mo *bis*-(pyranopterin guanine dinucleotide), or Mo-*bis*PGD, found in most prokaryotic molybdoenzymes. A [4Fe-4S] cluster and two *c*-type hemes form an intramolecular electron transfer chain that deliver electrons to the active site. Lysine 56 is a highly conserved amino acid which connects, through hydrogen-bonds, the [4Fe-4S] center to one of the pyranopterin ligands of the Mo-cofactor. This residue was proposed to be involved in the intramolecular electron transfer, either defining an electron transfer pathway between the two redox cofactors, and/or modulating their redox properties.

In this work, we investigated the role of this lysine by combining site-directed mutagenesis, activity assays, redox titrations, EPR and HYSCORE spectroscopies. Removal of a positively-charged residue at position 56 strongly decreased the redox potential of the [4Fe-4S] cluster at pH 8 by 230 mV to 400 mV in the K56H and K56M mutants, respectively, thus affecting the kinetics of electron transfer from the hemes to the [4Fe-4S] center up to 5 orders of magnitude. This effect was partly reversed at acidic pH in the K56H mutant likely due to protonation of the imidazole ring of the histidine. Overall, our study demonstrates the critical role of a charged residue from the second coordination sphere in tuning the reduction potential of the [4Fe-4S] cluster in *Rs*NapAB and related molybdoenzymes.

1. Introduction

Mononuclear molybdenum proteins constitute a large class of enzymes whose function is related to the presence of a molybdenum atom in their active site called the Molybdenum cofactor (Mo-cofactor). Among them, the largest family regroups enzymes featuring a Mo-*bis* (pyranopterin guanine dinucleotide) or Mo-*bis*PGD cofactor. An equivalent tungsten-containing cofactor (W-*bis*PGD cofactor) is alternatively found in a few enzymes of this family [1,2]. Mo/W-*bis*PGD enzymes are exclusively found in Prokaryotes. They mostly catalyze redox reactions involving transfer of an oxygen-atom, sulfur-atom or hydrogen-atom to or from a large variety of substrates such as nitrate, nitrite, DMSO, chlorate, arsenate, polysulfide, formate or carbon dioxide. They behave specifically either as oxidase or reductase, or reversibly for a few of them. Redox chemistry at the Mo-cofactor implies two one-electron transfer steps to or from the active site. Enzymes such as DMSO reductase (DmsA), TMAO reductase (TorA) or biotin-*d*-sulfoxide reductase (BisC) possess a Mo-*bis*PGD active site as a sole prosthetic cofactor and exchange electrons directly with their redox physiological partner [3]. All other Mo/W-*bis*PGD enzymes also hold in their catalytic subunit a Fe-S center, usually found as a [4Fe-4S] or rarely as a [3Fe-4S], which constitutes the first electron transfer relay to or from the active site.

Sequences alignment pointed out a highly conserved lysine residue in periplasmic nitrate reductases (Nap), assimilatory nitrate reductases (Nas) and formate dehydrogenases (Fdh), which are structurally and phylogenetically closely related [2,4]. In the crystal structure of FdhH from *Escherichia coli*, the first solved structure of a Mo/*W-bis*PGD

* Corresponding author at: Aix-Marseille Univ, CNRS, Laboratoire de Bioénergétique et Ingénierie des Protéines, UMR7281, F-13402 Marseille Cedex, France.
E-mail address: burlat@imm.cnrs.fr (B. Burlat).

https://doi.org/10.1016/j.bbabio.2019.01.003
Received 3 August 2018; Received in revised form 30 November 2018; Accepted 25 January 2019
Available online 29 January 2019
0005-2728/

enzyme, this Lys residue connects through hydrogen-bonds the extremity of one of the two pyranopterin ligands of the Mo-cofactor to the neighbor FeS center [5]. Later on, this conserved lysine was identified in all tridimensional structures of Fdh [6,7] and Nap [8–11], but also of ethylbenzene dehydrogenase (Ebdh) [12], perchlorate reductase (Pcr) [13] and acetylene hydratase (Ah) [14]. At the same position, an arginine is alternatively found in the crystal structures of membrane-bound nitrate reductase (Nar) [15,16], arsenite oxidase (Aio) [17,18] or polysulfide reductase (Psr) [19]. The only exception known so far is the tungsten-containing formylmethanofurane dehydrogenase (Fmd) from *Methanothermobacter wolfeii*, whose recent structure reveals an isoleucine in place of the Lys or Arg found in the other enzymes [20]. This positively-charged Arg or Lys residue was therefore proposed to be directly involved in the electron transfer pathway between the FeS center and the Mo-cofactor within the catalytic subunit Mo/W-*bis*PGD enzymes.

In *Escherichia coli* trimeric DMSO reductase (*Ec*DmsABC), replacement of arginine by a serine completely eliminated the quinol: DMSO oxidoreductase activity of the enriched membrane preparations while activity in the presence of benzyl viologen as an electron donor was retained [21]. The equivalent mutation (R96S mutant) studied in enriched membranes of *Ec*NarGHI led to similar observations consistent with the fact that arginine mutation affects intramolecular electron transfer process [22,23]. Furthermore, redox potential of the FeS center within the NarG catalytic subunit (also called FeS_0 in *Ec*Nar, see ref [24]) was decreased by about 115 mV in the R96S variant, which was interpreted as a consequence of the removal of the Arg residue positive charge [22]. In the soluble nitrate reductase from *Synechococcus* sp. PCC 7942, the conserved Lys in the vicinity of the [4Fe-4S] cluster (lysine 58) was mutated into arginine or glutamine [25]. Characterization of purified mutants revealed that both K58R and K58Q proteins are inactive and partially hold a FeS center that is furthermore degraded. This points out a structural role for the neighbor Lys in the FeS cluster incorporation and/or stabilization but does not provide any valuable information on a putative mechanistic role for this residue [25]. Mutation of equivalent Lys (at position 85) was also made in *Cupriavidus necator* (formerly *Ralstonia eutropha*) periplasmic nitrate reductase NapAB. Activity measurements on periplasmic extracts indicated that the conservative K85R mutant displays a nitrate reductase activity of 23% of the wild-type enzyme while the K85 M mutant is completely inactive for nitrate reduction [4]. Finally, other works on NapAB from *Rhodobacter sphaeroides* (*Rs*) suggest that the enzyme activity strongly depends on efficiency of electron transfer between the [4Fe-4S] cluster and the Mo-cofactor in which Lys may play an essential role [26]. Overall, the survey of the current literature shows the need for further biochemical and structural data in order to investigate the functional relevance of this conserved Lys residue within the Nap/Fdh subfamily.

In the present work, we address this issue on the periplasmic nitrate reductase NapAB from *R. sphaeroides*. *Rs*NapAB is a heterodimer made of a catalytic NapA subunit (89 kDa) and of an electron transfer NapB subunit containing two *c*-type hemes (18 kDa) (Fig. 1A) [9]. Lysine residue (K56) connects through hydrogen-bonds a [4Fe-4S] cluster located in the catalytic NapA subunit to the proximal pyranopterin moiety (*P*-PPT in Fig. 1B) of the Mo-cofactor. This iron-sulfur cluster is covalently bound to the protein matrix through a classical $C_{19}x_2C_{22}x_3C_{26}x_nC_{54}$ cysteine coordination motif. The K56R, K56M and K56H mutations were constructed and overexpressed in *R. sphaeroides*. We did not get any expression of the *Rs*NapAB enzyme for the K56R mutation. Biochemical and biophysical properties of the K56M and K56H mutated enzymes were investigated by the means of EPR spectroscopy combined to activity assays and potentiometric titrations. We found out that substitution of Lys with non-charged residues severely lowers the reduction potential of the $[4Fe\text{-}4S]^{2+/1+}$ center thus increasing the thermodynamic barrier from the hemes to the [4Fe-4S] center and impairing the kinetics of intramolecular electron transfer. Overall, the present study reveals that Lys strongly influences the redox properties of the [4Fe-4S] center through electrostatic secondary sphere coordination interactions.

2. Materials and methods

2.1. Bacterial strains and growth conditions

Rhodobacter sphaeroides f. sp. denitrificans IL106 was grown at 30 °C in Hutner medium [29] under semi-aerobic conditions (1.5 L of culture in 3 L Erlenmeyer flask, 150 rpm). *E. coli* strains were grown at 37 °C in Luria-Bertani medium. When necessary the medium was complemented with 25 μg·mL^{-1} Kanamycine and 50 μg·mL^{-1} streptomycin and spectinomycin for *R. sphaeroides* and 50 μg·mL^{-1} Kanamycine for *E. coli*. For NapAB expression, Hutner medium was supplemented with 1 mM IPTG.

2.2. Mutant construction, enzyme expression and purification

The NapAB complexes were overexpressed in a *R. sphaeroides* strain deleted for nitrate reductase [30] but bearing a pIND4 derivative plasmids containing *napAB* genes under the control of an IPTG-inducible promoter with a sequence coding for six histidines fused at the end of the *napB* coding frame. pSM211 (containing wild-type *napAB* genes) was constructed by *napAB* PCR amplification from pMS617 plasmid [30] with primers pINDnapA: 5′-aatcatgaccctcacacggcgcg-3′ and revpINDnapA: 5′-gcaagcttgtgatggtgatggtggt-3′. The PCR DNA fragment was digested with *Bsp*HI and *Hin*dIII and cloned into pIND4 previously digested with *Nco*I and HindIII. Plasmids pSM263 and pSM264 containing the sequences for expression of K56H NapAB and K56M NapAB enzymes, respectively, were obtained by site directed mutagenesis of pSM211. QuickChange II XL Site-Directed Mutagenesis kit from Stratagene was used to generate point mutations into NapA. pSM211 was amplified using PfuUltrahigh fidelity DNA polymerase and two complementary primers containing the desired mutation flanked by unmodified nucleotide sequence. For K56H mutant the following primers were used: NAPK56H (5′-GGCCTCAACTGCGTGCACGGCTATTTC CTGTCC-3′) and RevNAPK56H (5′-GGACAGGAAATAGCCGTGCACGCA GTTGAGGCC-3′). For K56M mutant: NAPK56M (5′-GGCCTCAACTGC GTGATGGGCTATTTCCTGTCC-3′) and RevNAPK56M (5′-GGACAGGAA ATAGCCCATCACGCAGTTGAGGCC-3′). For K56R mutant: NAPK56R (5′-GGCCTCAACTGCGTGCGGGGCTATTTCCTGTCC-3′) and Re-vNAPK56R (5′-GGACAGGAAATAGCCCCGCACGCAGTTGAGGCC-3′). After PCR amplification, the DNA was digested with *Dpn*I, which is specific for methylated DNA and is used to digest the parental DNA template. The nicked vector DNA incorporating the desired mutation was then transformed into *E. coli* DH5alpha competent cells. The insert was sequenced to control that selected clones contain the desired mutation. The resulting plasmids were moved from *E. coli* to *Rs napA* mutant MS523 by standard procedure. His-tagged wild-type and mutant NapAB complexes were overproduced and purified as previously described in ref [31].

2.3. Nitrate reductase assay

Nitrate reductase activity was assayed spectrophotometrically using reduced benzyl viologen (BV) as electron donor. All assays were performed anaerobically in an anaerobic chamber (JACOMEX glovebox, pO_2 < 3 ppm) equipped with a water-regulated cuvette-holder apparatus connected *via* optical fibers to a UV-MC2 spectrometer (Safas Instruments). Reactions were carried out at 25 °C in an optical cuvette filled with 875 μL of either 50 mM buffer acetate (pH 5), MES (pH 6) or HEPES (pH 7 and 8) containing 50 mM NaCl, 0.16 mM BV and from 5 to 25 nM of purified NapAB protein. A few microliters of a 30 mM freshly prepared dithionite solution was added to reduce BV to around 1 unit of absorbance. Reaction was started by addition of 100 μL of stock solution of potassium nitrate which concentration varied from 200 μM to 100 mM. The nitrate oxidation rate was derived from the measure of the

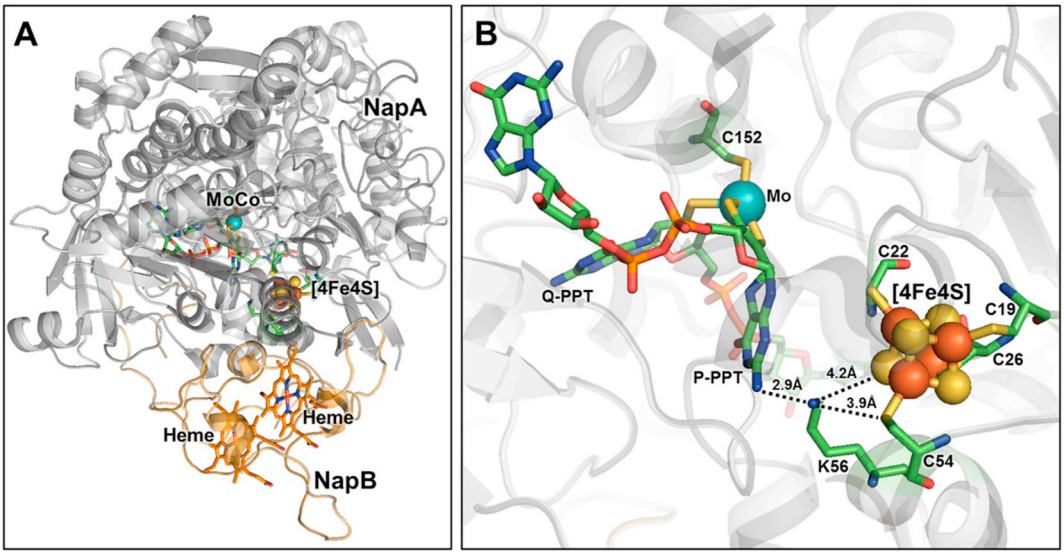

Fig. 1. (A) Overall structure of *Rhodobacter sphaeroides* NapAB (PDB 1OGY), at a resolution of 3.2 Å, made with the Pymol software. Backbone of the catalytic subunit NapA is represented in grey and those of the electron-transfer subunit NapB in gold. (B) Close-up of the Mo-cofactor and of the [4Fe-4S] cluster. P-PPT refers to the pyranopterin that is proximal to the iron-sulfur cluster and Q-PPT to the pyranopterin that is distal to it [24]. One can notice that the sixth ligand of the molybdenum ion, first assigned in the crystal structure of *D. desulfuricans* (*Dd*) NapA to an oxo or hydroxo [8], then reassigned to a sulfide ligand in latter structures from *Dd*NapA [27], *Cupriavidus necator* NapAB [11] or from theoretical works [28], was not resolved in the crystal structure of *Rs*NapAB [9].

tangent to the recorder trace at the start of the reaction, using an absorption coefficient ε_{600nm} of 10.4 mM^{-1} cm^{-1} for the reduced BV.

2.4. Metal content, redox titrations and EPR spectroscopy experiments

Metal content of NapAB enzymes was measured by using ICP-MS analysis (spectrometer HP 4500, calibrated using an external standard). Potentiometric titrations were performed as previously described in an anaerobic cell flushed with a stream of wet argon [32]. The cocktail of mediators was composed of 2,6-dichlorophenolindophenol, 2,5-dimethyl-p-benzoquinone, 1,2-naphtoquinone, phenazine methosulfate, phenazine ethosulfate, methylene blue, 2,8-dihydroxyphenoxazine, indigo-disulfonate, 2-hydroxy-1,4-naphtoquinone, 3,7-diamino-5-phenylphenazinium chloride, 3-amino-7-dimethylamino-2-methylphenazine hydrochloride and methyl viologen dichloride. The mediator cocktail was added to a final concentration of 5 µM while the enzyme concentration varied from 20 to 40 µM, depending on the preparation, in a 50 mM Hepes/NaCl solution buffered at pH 8 and 300 mM Mes/NaCl at pH 6. Continuous wave experiments were performed on a Bruker Elexsys E500 spectrometer fitted with an Oxford Instruments ESR-900 helium-gas flow. Continuous wave EPR saturation experiments were analyzed using the empirical model developed by Rupp et al. [33]. Saturation data were fitted to Eq. (1) in order to take into account the inhomogeneous broadening of the EPR linewidth:

$$S = \frac{\sqrt{P}}{\left(1 + \frac{P}{P_{1/2}}\right)^{0.5b}} \quad (1)$$

In this equation, S represents the first derivate of the absorption resonance, P is the incident microwave power, $P_{1/2}$ is the half-saturation power and b an inhomogeneity factor. Spin-lattice relaxation times T_1 characterizing the [4Fe-4S] center were deduced from the relaxation broadening of the high-field (g_x) peak. The half-width $\delta_L = \hbar / (g\beta T_1)$ of the Lorentzian relaxation component was determined as described before [34,35] by comparing the experimental spectrum with a calculated spectrum resulting from the convolution of the low temperature spectrum (recorded at 15 K) with a Lorentzian line of half-width δ_L.

2.5. Pulsed-EPR spectroscopy

X band pulsed EPR experiments were carried out on a Bruker Elexsys E580 spectrometer equipped with a dielectric ring resonator (ER4118X-MD5) and a helium flow cryostat (Oxford CF935). The microwave pulses were amplified with a 1 kW TWT amplifier. Electron Spin Echo Field Sweep (ESE-FS) two-pulse experiment ($\pi/2$–τ–π–τ–echo) was measured as a function of magnetic field at fixed time interval of 200 ns between the two microwave pulses ($\pi/2$ = 16 ns). The HYSCORE measurements were performed at a temperature of 15 K. A conventional two-dimensional (2D) four-pulse sequence ($\pi/2$–τ–$\pi/2$–t1–π–t2–$\pi/2$–τ–echo) [36] was applied with a τ delay of 136 ns (or 204 ns for the experiments displayed in Fig. SI-1) and a 32 ns detector gate, centered at the maximum of the echo signal. 2D HYSCORE spectra were recorded at magnetic fields of 355.3 mT (microwave frequency of 9.687 GHz, 11 averaged scans for the wild-type NapAB), 356.7 mT (microwave frequency of 9.687 GHz, 11 averaged scans for the K56M mutant) and 356.1 mT (microwave frequency of 9.703 GHz, 10 averaged scans for the K56H mutant). These magnetic fields correspond to the g_y of the ESE-FS. The nominal duration of the $\pi/2$ pulse was 12 ns. The π pulse of 24 ns was optimized using a nutation experiment. The echo intensity was measured as a function of t_1 and t_2, incremented in steps of 16 ns from the initial value of 24 and 32 ns, respectively. HYSCORE data were collected in the form of 2D time-domain patterns as a 256 × 256 matrix at a repetition rate of 2000 Hz. An 8-step phase cycling procedure was used to remove unwanted echoes. Spectral processing was performed using a home-written Matlab® routine. The 2D time domain data were corrected for the unmodulated relaxation decay by a third-order polynomial background in both dimensions. Each time domain slices were apodized using a Hamming window function, zero-filled to 1024 points and Fourier transformed in both dimensions. The frequency maps were plotted as contour plot of the amplitude (absolute values).

3. Results

3.1. Kinetic characterization of the purified K56 mutants

Three variants of Lysine 56 were constructed and the resulting

Table 1
Purification yield, metal content and kinetic properties of the wild-type nitrate reductase, K56M and K56H variants from *R. sphaeroides*. Due to the poor production of the K56H mutant and to the very low enzyme activity at alkaline pH, *K*m for nitrate could not been determined at pH 7. Activity of the K56M mutant could not been determined at pH 5 because the catalytic rate for nitrate oxidation was very low in comparison with autoxidation of reduced BV that was not negligible at acidic pH as seen in control experiments.

NapAB	Purification yield (mg of protein/L of culture)[a]	*Relative 6Mo/*Fe *content (ICP-MS)*	*K*m (μM)			k_{cat} (s^{-1}) at pH 6	k_{cat}/*K*m at pH 6
			pH 5	pH 6	pH 7		
Wild-type	3 ± 1	0.95 ± 0.10	50 ± 20	170 ± 20	250 ± 50	61 ± 2	360 ± 50
K56H	0.8 ± 0.5	0.80 ± 0.10	110 ± 20	140 ± 40	nd	22 ± 1	155 ± 50
K56M	1.7 ± 0.7	0.90 ± 0.10	nd	10 ± 5	75 ± 25	2.5 ± 0.5	250 ± 50

[a] Average of three purification batches. nd: not determined.

NapAB enzymes were overexpressed in *R. sphaeroides*. We replaced Lys56 1) with Arg that is found at this position in several Mo-*bis*PGD 3D structure, 2) with Met in order to keep the side-chain length of the residue and suppress the positive charge and hydrogen-bonding to the FeS center, and finally 3) with His thus removing the positive charge from the imidazole ring at alkaline pH. Surprisingly, the conservative K56R mutation did not express in *R. sphaeroides* while the equivalent K95R mutation in *Ralstonia eutropha* Nap led to periplasmic extracts retaining nitrate reductase activities [4]. Production and purification of the variants in *R. sphaeroides* gave yields of 1.7 mg and 0.8 mg of purified protein per liter of *R. sphaeroides* culture for the K56M and K56H, respectively, against 3 mg for the wild-type enzyme. Inductively Coupled Plasma – Mass Spectrometry (ICP-MS) experiments provide an estimate of the metal content in the purified NapAB samples. For both mutants, we found a relative metal content of around 1 Mo atom to 6 Fe atoms as usually found for the wild-type enzyme (Table 1). Nitrate reduction activity was assayed spectrophotometrically for the wild-type NapAB enzyme and K56H and K56M mutants (Tables 1 and SI.1). Specific nitrate reductase activity of the wild-type enzyme in the presence of reduced benzyl viologen serving as electron donor produced a *V*max value of 24 ± 4 μmol·min^{-1}.mg^{-1} and a *K*m for nitrate of 250 μM at pH 7, data which are comparable to those previously obtained in the presence of reduced methyl viologen (25 μmol·min^{-1}·mg^{-1} and 170 μM) [9]. Comparatively, both mutants displayed decreased activities at pH 7 (5% and 11% of the wild-type activity for K56M and K56H mutants respectively) thus indicating that the mutation is critical for enzymatic activity. Fig. 2 shows the pH dependence of the specific nitrate reductase activity for the wild-type enzyme and mutants in a pH range in between 5 and 8. All measurements have been made in the presence of saturating nitrate concentrations (2.5 and 5 mM). Wild-type enzyme displayed a bell-shaped profile with a maximum of activity at pH 6 (34 ± 1 μmol·min^{-1}·mg^{-1}) and a four-fold decrease at higher pH (7.8 ± 0.9 μmol·min^{-1}·mg^{-1} at pH 8). Specific activities of K56H and K56M mutants revealed very different pH profiles. Specific activity of the K56M mutant did not depend on pH (averaged value of 1.1 ± 0.1 μmol·min^{-1}·mg^{-1}) over the domain of pH investigated. In contrast, the specific activity of K56H varied as a function of pH with a maximum of activity of about 40% of the wild-type enzyme at pH below 6. To go further into the kinetic characterization of the mutants and of the wild-type NapAB enzymes, the apparent Michaelis constant *K*m was determined from colorimetric assays at various nitrate concentration and for a pH ranging from 5 to 7. We found that the *K*m for the wild-type enzyme increases with pH, as found before from Protein Film Voltammetry experiments (unpublished results). K56H mutant displays a *K*m for nitrate that is similar to the one found for the wild-type (140 μM *vs* 170 μM at pH 6) whereas K56M mutant presents a lower *K*m (10 μM *vs* 170 μM at pH 6).

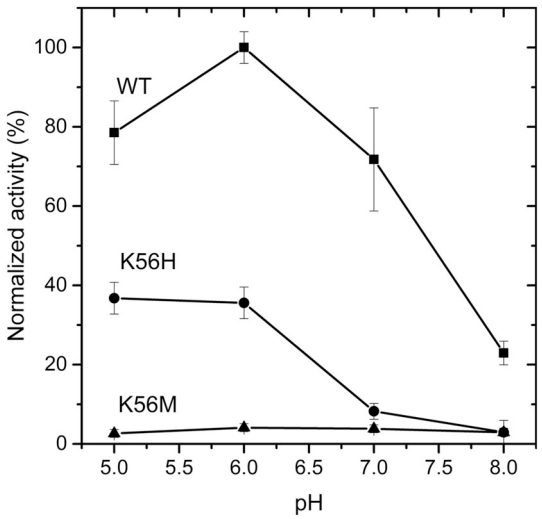

Fig. 2. Normalized nitrate reductase specific activity as function of pH of the buffered solution for the wild-type nitrate reductase NapAB (■), K56H (●) and K56M (▲) mutants from *R. sphaeroides*. The specific nitrate reductase activities (V_{max}) were expressed in μmole of consumed nitrate per minute and per mg of enzyme and normalized towards the maximum activity measured for the wild-type enzyme (that is 34 μmol·min^{-1}·mg^{-1} at pH 6). Activities were determined in solution in the presence of either 2.5 mM or 5 mM nitrate and 120 μM of reduced benzyl viologen and at 30 °C. Assays were performed in duplicate with an enzyme concentration of 6.6 nM (wild-type enzyme), 9.5 nM (K56H mutant) and 25 nM (K56M mutant).

3.2. Electronic and structural properties of the metal cofactors in the K56 mutants as deduced from EPR spectroscopy experiments

We used continuous wave X-band EPR spectroscopy for probing the influence of the K56 mutation on the structure of the metallic centers in the K56M and K56H mutants. In the wild-type NapAB protein purified in aerobic (*i.e.* oxidized) conditions, the *c*-type hemes from the NapB subunit are oxidized (Fe^{III}, $S = 1/2$) and give a rhombic EPR spectrum detected at low temperature with *g*-values at 2.94, 2.28 and 1.49 (15 K in Fig. 3A). A similar EPR signal accounting for two hemes per NapAB was observed in both K56M and K56H mutants, showing then that the structure of the hemes is not affected by the mutation. Their *g*-values exhibit slight variations likely due to small changes of the relative angle between the imidazole rings of the heme axial histidine ligands induced by the mutation (Table 2) [37]. Air-purified wild-type enzyme preparations also display the so-called “high *g* resting” Mo(V) rhombic EPR signal around $g \sim 2$ coming from a sub-stoichiometric fraction of the Mo-cofactor (Fig. 3B). This signal represents 2–20% of the enzyme, depending on protein preparation. Similar “high *g* resting” Mo(V) signal was also observed in both K56 mutants in variable ratio which were not exceeding 5% for K56M and 10% for K56H. The lower resolution of the low field peaks results from a slight decrease of the *g*-tensor anisotropy in the mutants. No other Mo(V) EPR signal was detected in the air-purified K56 mutants. In NapAB, the $[4Fe\text{-}4S]^{2+/1+}$ cluster is paramagnetic in its reduced state with $S = 1/2$. Fig. 3C shows the rhombic signal associated to the dithionite-reduced $[4Fe\text{-}4S]^{1+}$ cluster in the

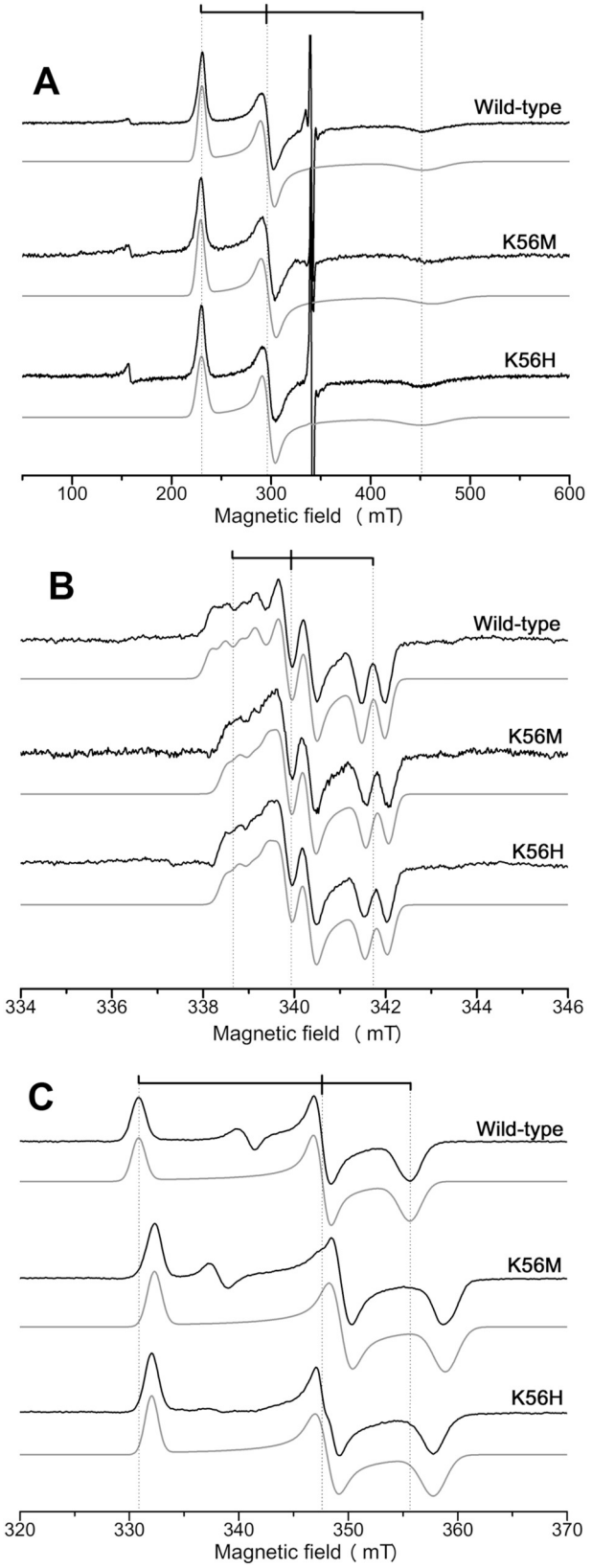

Fig. 3. X-band EPR signatures of the metal cofactors in the wild-type NapAB, K56M and K56H mutants from *R. sphaeroides*. (A) Signatures of the *c*-type hemes detected in the as-prepared (air-oxidized) state of NapAB. (B) "High *g* resting" Mo(V) EPR signal that is also visible in the as-prepared state of NapAB. (C) Signature of the $[4Fe\text{-}4S]^{1+}$ center detected in the dithionite-reduced state of NapAB. Enzyme concentration was 80 μM for wild-type enzyme, 65 μM and 70 μM for the K56M and K56H mutants, respectively. The reduced state of the sample was obtained by adding a small volume of a concentrated and buffered dithionite solution at a final concentration of 2.5 mM. Experimental parameters: microwave frequency 9.475 GHz, temperature 15 K (A, C) and 55 K (B), modulation amplitude 2 mT (A), 0.2 mT (B) and 1 mT (C), microwave power 4 mW (A), 1 mW (B, C), number of scans averaged 1 (A), 9–64 (B), 1–4 (C). The experimental traces were simulated by using the EasySpin software package [44] with the parameters given in Table 2.

wild-type enzyme with *g*-values at 2.042,1.947 and 1.901. Surprisingly, we could not detect any iron-sulfur EPR signal in the K56 mutants when the samples were incubated with for less than 5 min prior to freezing of the EPR tube and EPR recording. In the meantime, the hemes from the NapB subunit were immediately reduced as judged from the disappearance of their EPR signal (*vide infra*). Achievement of a quantitative EPR signal was effective only after subsequent incubation with an excess of dithionite (from 50 to 90 equivalents of protein) for at least 1 h for both mutants. In these conditions, we recorded a rhombic signal that is slightly more anisotropic than that of the wild-type enzyme (Fig. 3C). Changes in *g*-values caused by Lys mutation are moderate and indicate that the overall structure of the FeS cluster is essentially unchanged. For both mutants, EPR linewidths are broader than those of the wild-type enzyme. This is attributed to an increase of the *g*-strain effect and probably reflects an increase of the local flexibility of the protein due to Lys mutation. Comparison of EPR signal intensity of the dithionite-reduced $[4Fe\text{-}4S]^{1+}$ center and of an external copper standard gave 0.7 and 1 $[4Fe\text{-}4S]^{1+}$ center/protein for the K56M and K56H mutants, respectively.

We determined the influence of Lys mutation on the electronic properties of the [4Fe-4S] center by studying the microwave power saturation of the EPR signal at 15 K. A log-log representation of $S/P^{1/2}$ (*i.e.* the EPR signal amplitude over the square root of the microwave power) against the microwave power *P* is given in Fig. 4A for the wild-type, K56H and K56M proteins. Saturation curves for the three enzymes were analyzed with the empirical Rupp equation (see Materials and methods) that considers the power of half-saturation ($P_{1/2}$) and the degree of homogeneous/inhomogeneous broadening parameter (*b*). All saturation curves were adjusted manually to experimental data with a same inhomogeneity parameter *b* of 1.65 that was found higher than the value of 1.22 previously reported for [4Fe4S]-containing proteins [33]. The $[4Fe\text{-}4S]^{1+}$ center presents fairly similar saturation behavior at 15 K in the wild-type enzyme and K56H mutant with $P_{1/2}$ values of 2.7 and 2.3 mW respectively, while its displays faster relaxation properties in the K56M mutant ($P_{1/2}$ = 15 mW). Relaxation broadening of the EPR linewidth experiments allow measuring the spin-lattice relaxation time T_1 of the $[4Fe\text{-}4S]^{1+}$ cluster. Spectral broadening of the $[4Fe\text{-}4S]^{1+}$ signal was studied in the temperature range from 15 to 80 K. Relaxation broadening measurements were performed on the high-field (g_x) peak of the EPR signal. By comparison to the wild-type and the K56H mutant, the $[4Fe\text{-}4S]^{1+}$ signal of the K56M mutant starts to broaden at a lower temperature (20K), which confirms the faster relaxation properties of the cluster in this mutant. Thus, both microwave power saturation and relaxation broadening experiments exhibit some perturbation of the spin-lattice relaxation of the [4Fe-4S] center upon Lys mutation. This results in an enhancement of the spin-lattice relaxation in the K56M mutant and a slight decrease in the K56H mutant. Spin-lattice relaxation time T_1 was deduced from measurement, at each temperature, of the half-width δ_L of the Lorentzian relaxation component, accordingly to the relation $\delta_L = \hbar / (g\beta T_1)$, see Fig. 4B and Materials and methods. Temperature dependence of the relaxation rate $1/T_1$ was analyzed using the equation $1/T_1 = \exp(-\Delta/k_B T)$ which corresponds to an Orbach process involving a low-lying excited state of energy Δ. We measured some Δ values of 165 ± 5, 210 ± 15 and 110 ± 10 cm^{-1} for the wild-type, K56H and K56M enzymes,

Table 2
g- and *A*-parameters for the *c*-type hemes, the $[4Fe\text{-}4S]^{1+}$ and the Mo(V) "high *g* resting" species in wild-type, K56M and K56H NapAB enzymes from *R. sphaeroides*. The given parameters are those determined in the simulations of the EPR spectra by using the EasySpin software package [44]. For the hemes and the $[4Fe\text{-}4S]^{1+}$ signals, *g*-strain values are indicated in brackets. For the Mo(V) "high *g* resting" signal, linewidths were simulated using a *H*-strain of 0.30 mT. Splitting of the Mo(V) signal corresponds to hyperfine interaction with two non-exchangeable $I = 1/2$ nuclei attributed to the β-methylene protons of the cysteine that binds the molybdenum ion [45]. nd: not determined.

NapAB	Hemes $g_{z\ y,\ x}$	Mo(V) "high *g* resting" $g_{z\ y,\ x}$ and $A_{z\ y,\ x}$	$[4Fe\text{-}4S]^{1+}$ $g_{z\ y,\ x}$
Wild-type	2.94(0.118), 2.28(0.095), 1.49(0.146)	$g_{z\ y,\ x}$: 1.9990, 1.9907, 1.9810 $A_{z\ y,\ x}$: 0.65, 0.52, 0.50 $A'_{z\ y,\ x}$: 0.31, nd, nd	2.042(0.0083),1.947(0.0067),1.901(0.0089)
K56M	2.95(0.117), 2.27(0.103), 1.46(0.146)	$g_{z\ y,\ x}$: 1.9972, 1.9907, 1.9805 $A_{z\ y,\ x}$: 0.61, 0.50, 0.49 $A'_{z\ y,\ x}$: 0.30, nd, nd	2.037(0.0094), 1.938(0.0108), 1.886(0.0134)
K56H	2.94(0.141), 2.27(0.089), 1.49(0.158)	$g_{z\ y,\ x}$: 1.9973, 1.9907, 1.9806 $A_{z\ y,\ x}$: 0.61, 0.50, 0.48 A'$_{z\ y,\ x}$: 0.30, nd, nd	2.039(0.0083), 1.945(0.0109), 1.892(0.0135)

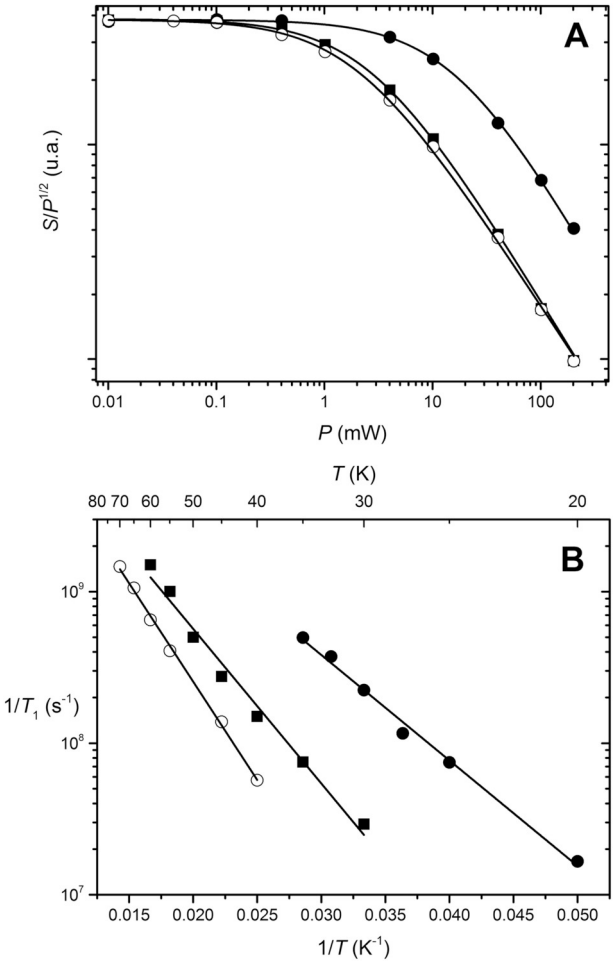

Fig. 4. Relaxation properties of the $[4Fe\text{-}4S]^{1+}$ center in the wild-type NapAB (■), K56H (o) and K56M (●) mutants from *R. sphaeroides*. Graph A presents the continuous wave microwave power saturation of the $[4Fe\text{-}4S]^{1+}$ center at 15 K. A log-log representation of the EPR signal amplitude (*S*) over the square root of the microwave power (*P*) against the microwave power *P* is plotted. Saturation curves were analyzed with the empirical Rupp equation (see Materials and methods) with an inhomogeneity parameter *b* of 1.65 and some half-saturation power values ($P_{1/2}$) of 2.7, 2.3 and 15 mW for the wild-type, K56H and K56M respectively. Graph B presents the temperature dependence of the spin-lattice relaxation rate of the $[4Fe\text{-}4S]^{1+}$ center between 20 and 65 K which are deduced from relaxation broadening experiments.

respectively. These Δ values are similar to those found in typical [4Fe-4S] centers [38,39], but the lower value found in the K56M mutant reveals some modifications of the exchange couplings between the iron ions within the cluster. This change is likely due to some weak distortions of the cubane structure induced by the mutation of the neighbor Lys56, an effect that was also observed in other kind of iron-sulfur centers upon variation of their coordination environment [34,35,40].

In order to investigate further modifications of the structural environment of the [4Fe-4S] center related to Lys mutation, we performed Hyperfine Sub-level Correlation (HYSCORE) spectroscopy experiments on NapAB enzymes at pH 8 in order to detect some weak magnetic hyperfine interactions between the $[4Fe\text{-}4S]^{1+}$ cluster and nearby magnetic nuclei. X-band HYSCORE spectra were recorded at the temperature of 15 K for which the spin-lattice relaxation of the $[4Fe\text{-}4S]^{1+}$ is slow enough to allow recording of pulsed EPR experiments. The set of experiments displayed in Fig. 5 were recorded with an interpulse delay of 136 ns optimized for the detection of the coupling with nitrogen nuclei. Superimposition of HYSCORE experiments on Fig. 5 shows for each mutant that the 2D-spectrum (black line) is very similar to that of the wild-type enzyme (red line). The low frequency region of the HYSCORE spectrum, close to the Larmor frequency of ^{14}N nucleus, recorded at the g_y resonant line displays well-resolved frequencies in the (+ +) quadrant (Fig. 5A and C). In this quadrant, off-diagonal cross-peaks are present at [3.85, 3.27] and [4.25, 3.66] MHz. Shape and position of these peaks are insensitive to the fields and τ delays and are therefore characteristic of double quantum coherence ($\Delta m_I = 2$) nuclear transitions associated to a ^{14}N nucleus (spin $I = 1$). These lines have a maximum intensity at a frequency that is well described by Eq. (2) [41,42]:

$$\nu_{dq\pm} = 2[\nu_{ef\pm}^2 + c]^{1/2} \quad (2)$$

with $\nu_{ef\pm} = |\nu_I \pm A_{iso}/2|$, in which ν_I is the ^{14}N nuclear Larmor frequency, A_{iso} is the isotropic hyperfine coupling constant and $c = \kappa^2(3 + \eta^2)$, where κ is the quadrupole coupling constant and η is the asymmetry parameter of the electric field gradient. Thus, the cross-peaks at [3.85, 3.27] and [4.25, 3.66] MHz in the (+ +) quadrant are tentatively attributed to $\nu_{dq\pm}$ of two ^{14}N nuclei labeled N_I and N_{II}. Using Eq. (2), this gives N_I ($A_I = 0.47$ MHz and $c_I = 1.93$ MHz^2) and N_{II} ($A_{II} = 0.53$ MHz and $c_{II} = 2.66$ MHz^2), respectively. The *c* values lead to an estimation of kappa ranging from 0.7 to 0.9 MHz, which is compatible with N nuclei from peptide chain [43].

A $I = 1/2$ nucleus such as ^1H produces correlation cross-peaks in the HYSCORE spectrum whose coordinates are the nuclear frequencies [$\pm\nu_\alpha$, $\pm\nu_\beta$] from opposite electron spin manifolds [41]. In the proton Larmor frequency region (around 15 MHz), a broad spot associated to several weakly-coupled ^1H-nuclei is observed whose shape is globally not affected by the Lys mutation (Fig. 5). In order to emphasize the detection of coupling with protons, we repeated the experiments shown

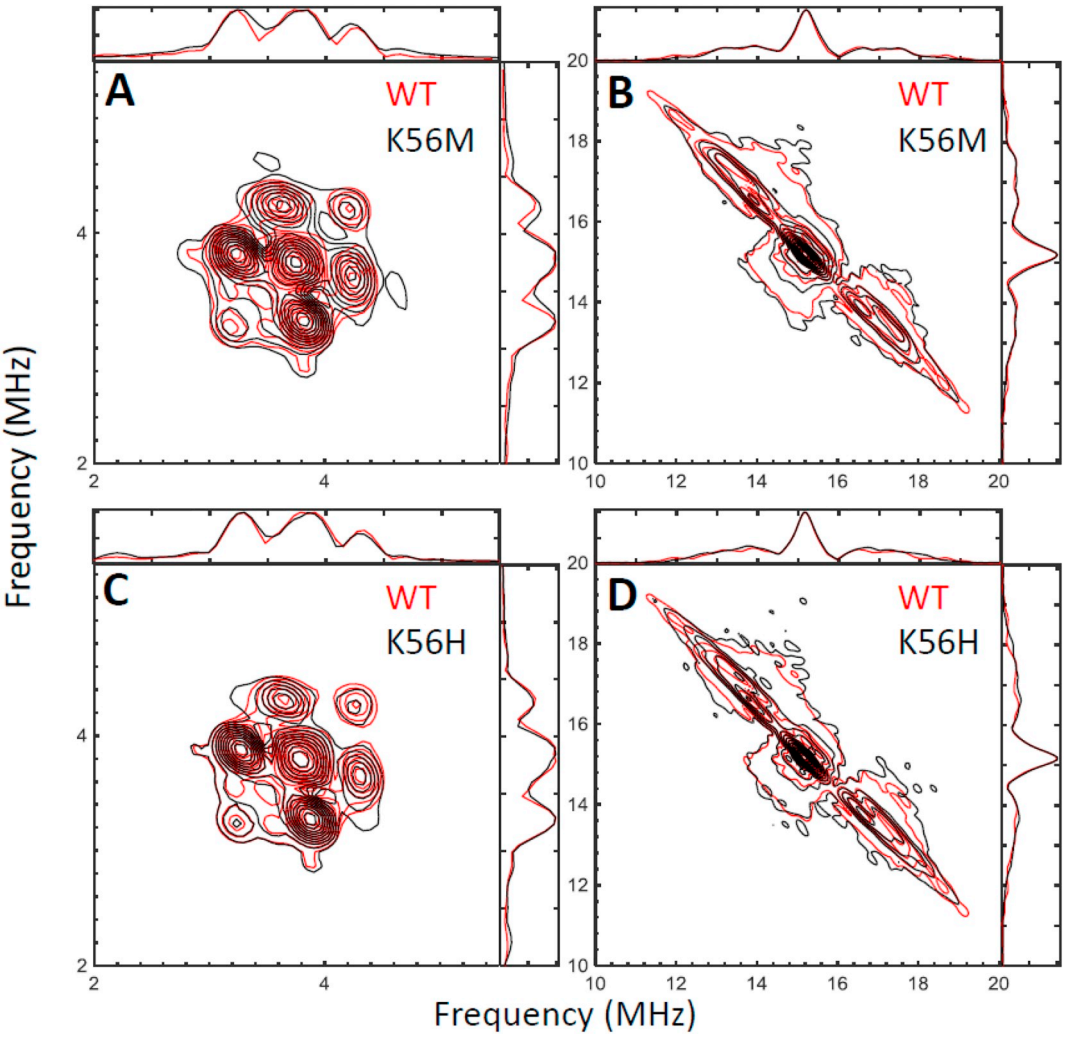

Fig. 5. X-band ^{14}N-HYSCORE (A, C) and ^{1}H-HYSCORE (B, D) spectra at pH 8 of the $[4Fe\text{-}4S]^{1+}$ center in the reduced wild-type NapAB (traces in red), K56H and K56M mutants (traces in black) from *R. sphaeroides*. Superimposition of the K56M and wild-type traces (A, B), superimposition of K56H and WT traces (C, D). Experimental parameters: temperature 15 K, time delay between first and second pulses t = 136 ns, microwave frequency: 9.687 GHz (wild-type, K56M) and 9.703 GHz (K56H), averaged scans: 11 (wild-type, K56M) and 10 (K56H), magnetic field 355.3 mT (wild-type), 355.7 mT (K56M), and 356.1 mT (K56H). Enzyme concentration was 60 µM for the wild-type enzyme and 70 µM for both the K56M and K56H mutants. Protein samples were reduced by adding small aliquots of a concentrated buffered dithionite solution to a final dithionite concentration of 2.5 mM.

in Fig. 5 with an interpulse delay of 204 ns (Fig. SI-1) for the wild-type and the K56M mutant. This further confirms the similarity of the HYSCORE spectra notably around the ^{1}H Larmor frequency. In conclusion, mutation of Lys56 shows no evident spectral changes in the proton frequency region that could be interpreted in relation with hydrogen-bonding modification around the reduced FeS center.

3.3. Kinetic and thermodynamic properties of K56M and K56H mutants

As mentioned above, we found that the complete chemical reduction of the $[4Fe\text{-}4S]^{2+/1+}$ center and the appearance of its EPR signal was surprisingly very slow (more than 1 h) in both K56M and K56H mutants. Fig. 6 shows the evolution of the EPR signals amplitude of the hemes, the "high *g* resting" Mo(V) and the $[4Fe\text{-}4S]^{1+}$ cluster, as a function of incubation time with an excess of dithionite (50 to 80 equivalents of enzyme). To do so, a small volume of dithionite solution (to a final concentration of 5 mM) was added directly to the protein sample (from 60 to 90 µM) kept in an EPR tube at room temperature under Ar atmosphere. The sample was incubated for a certain time before freezing and monitoring EPR spectra of the different redox centers. The EPR tube was then allowed to defrost under Ar for a longer incubation time before freezing and subsequent EPR recording. In wild-type *Rs*NapAB, chemical reduction of the electron transfer chain (hemes and FeS center) is fast enough to ensure full reduction of the hemes and of the [4Fe-4S] center after a short incubation time with dithionite (less than 1 min). In contrast, the Mo(V) "high *g* resting" species slowly disappears with a half-time constant ($t_{1/2}$) of 15 min at 25 °C in the wild type enzyme (Fig. 6). This unusual behavior was interpreted before as due to an activation process from a fraction of the enzyme (showing the Mo(V) "high *g* resting" signal) that slowly and irreversibly converts into an active form upon reduction [26,46]. In the K56H mutant, complete appearance of the $[4Fe\text{-}4S]^{1+}$ signal required 1 h à 25 °C ($t_{1/2}$ = 10 min) while the hemes signals disappeared rapidly in the same conditions (Fig. 6). This behavior was even more pronounced in the K56M mutant with an apparent reduction half-time constant $t_{1/2}$ of 50 min for the [4Fe-4S] cluster (Fig. 6). In the meantime, intensity of the "high *g* resting" Mo(V) signal decayed with $t_{1/2}$ of 20 ± 5 min for K56H similar to that of the wild-type, and with $t_{1/2}$ of 50 min for K56M (Table 3). This gives rate constants for the reduction of the [4Fe-4S] cluster of $k_{K56H} = 10^{-3}\,s^{-1}$ and $k_{K56M} = 2.10^{-4}\,s^{-1}$ that are much slower that the turnover rates of above $2\,s^{-1}$ measured at pH 8 for the mutants (Table SI.1) in the presence of viologen used as electron donor.

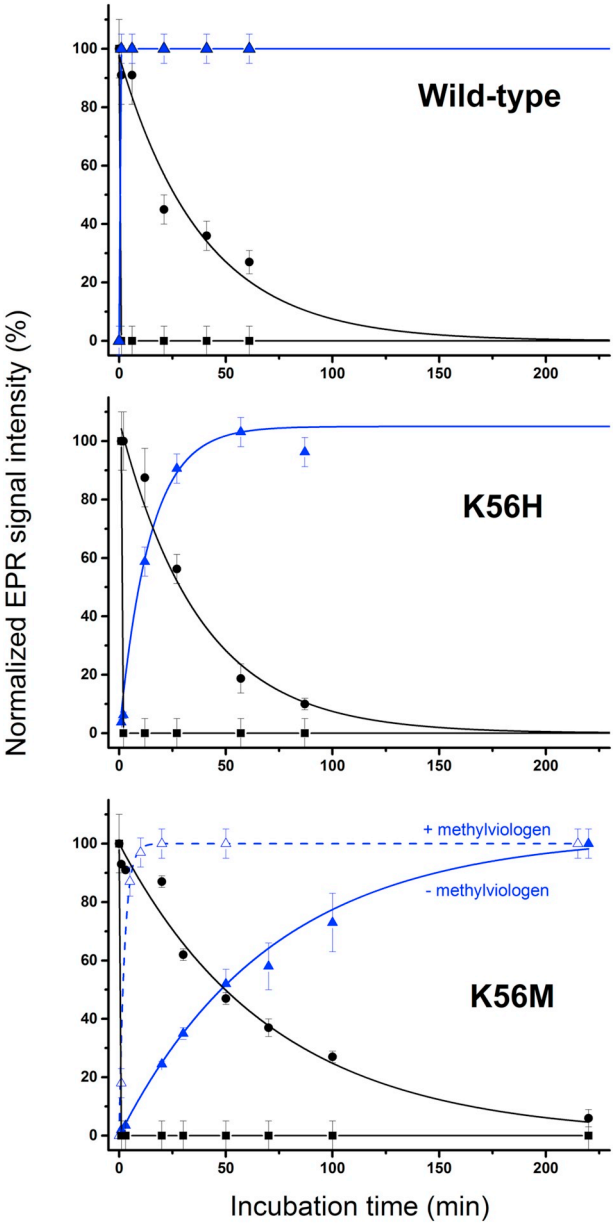

Fig. 6. Evolution of the EPR signal amplitude of the hemes (■), $[4Fe\text{-}4S]^{1+}$ (▲) and Mo(V) "high *g* resting" (●) as function of the incubation time with dithionite in the wild-type NapAB, K56H and K56M enzymes from *R. sphaeroides*. Kinetics of apparent reduction of the [4Fe-4S] center and of the Mo(V) were fitted with a pseudo-first order kinetics whose half-time constants are reported in Table 3. For the K56M mutant, the experience was reproduced in presence of a redox mediator (methylviologen at a final concentration of 5 μM). The corresponding data are plotted for the reduction of the [4Fe-4S] center only (△).

We explain this apparent contradiction below. We found that the reduction of the FeS cluster could be made faster by adding a redox mediator such as methylviologen (at a final concentration of 5 μM) (Table 3). Three electron routes to the [4Fe-4S] center can be envisaged: dithionite may deliver electrons to the [4Fe-4S] center *via* either the Mo-cofactor, or through the hemes, or directly from the surface of the protein. We have shown before that dithionite could not give electrons directly to the Mo-cofactor of *Rs*NapAB, probably due to the shape of the access funnel [32]. A direct electron transfer from dithionite to the [4Fe-4S] cluster seems unlikely considering the location of the [4Fe-4S] cluster within the NapAB dimer. Therefore, the most favorable electron route from dithionite to [4Fe-4S] center passes through the hemes from NapB. The results above could be rationalized with the help of a simple kinetic model developed in SI which only considers the reversible electron transfer between the hemes and the FeS center and the reduction of the hemes by an electron donor. In the framework of this model, the reduction rate (*k)* of the [4Fe-4S] cluster can be written according to Eq. (3):

$$k = k_r \exp \frac{F\Delta E^{\circ}}{RT} \tag{3}$$

k_r is the intermolecular electron transfer rate between the reductant and the hemes. $\Delta E^{\circ} = E^{\circ}_{FeS} - E^{\circ}_{heme}$ is the potential difference between the FeS center and the hemes. Thus the reduction rate *k* of the [4Fe-4S] center depends on thermodynamics of the intramolecular electron transfer. It is also proportional to the rate of reaction with the reductant in solution, which is consistent with the observation that addition of small quantities of methylviologen quickens the rate of apparition of the reduced cluster. We describe in SI a simple catalytic model including the intramolecular electron transfer. We show that, for this model, the catalytic rate under saturating nitrate concentration is not related to the rate of the apparition of the reduced [4Fe-4S], and can be significantly faster, reflecting that the state in which the protein is fully reduced is not necessarily an intermediate in the catalytic cycle. Besides, catalysis can be rate-limited by the reduction of the hemes (rate k_r). Our experiments show that the reduction rate of the protein k_r is strongly dependent on the nature of the electron donor (dithionite or viologen) with k_r (dithionite) much lower than k_r (viologen). This can be another factor to explain the large difference in rates, since the reduction rate *k* of the [4Fe-4S] cluster measured in the kinetic experiments monitored by EPR with dithionite as electron donor are much slower than turnover rates found in activity assays done in the presence of 160 μM benzylviologen.

In order to fully understand the unexpected slow reduction of the [4Fe-4S] cluster under non-turnover conditions, we performed potentiometric titrations of the redox centers in the wild-type enzyme and the K56 variants at pH 8. Redox titration curves for the hemes are given in fig. SI.3 and show for both mutants that Lys mutation impacts only slightly the redox properties of the hemes at pH 8 (Table 3). Conversely, the reduction potential associated to the [4Fe-4S] cluster exhibits a spectacular decrease, going from −110 mV in the wild-type enzyme to −340 mV and −520 mV in the K56H and K56M mutants, respectively (Fig. 7). Thus, substitution of Lys with non-charged residues (both Met and His should be neutral at pH 8) has a major effect on the reduction potential of the [4Fe-4S] center. We performed the redox titrations at pH 6 for the wild-type enzyme and the K56H mutant (Fig. SI.5). The reduction potential $E^{\circ\prime}$ value obtained for the [4Fe-4S] cluster in the WT enzyme (−95 mV ± 10 at pH 6) was found rather close from the value of −110 ± 10 mV found at pH 8. In contrast, the $E^{\circ\prime}$ for the [4Fe-4S] cluster in the K56H mutant shows a very large pH-dependence with $E^{\circ\prime} = -145 \pm 20$ mV at pH 6 against −340 mV ± 10 at pH 8 (average of two experiments for both pH). This suggests that protonation of His has a strong influence on the redox properties of the FeS cluster and could explain the partial recovery of the enzyme activity observed at low pH in this mutant.

4. Discussion and conclusion

The aim of this work was to investigate the role of a conserved positively-charged Arg or Lys residue that is present within the catalytic subunit of virtually all Mo-*bis*PDG enzymes and that is located in between the Mo-cofactor and the proximal iron-sulfur center. In *Rs*NapAB catalytic subunit, this residue corresponds to a lysine that connects through hydrogen-bonds the extremity of one pyranopterin moiety of the Mo-cofactor to a [4Fe-4S] center. Its position has suggested that it could be directly involved in the intramolecular electron transfer process, either mediating electron transfer between the two metal centers, or modulating their redox properties [4,5,22,25]. Three NapAB

Table 3
Apparent half-time constant $t_{1/2}$ (min) for the [4Fe-4S] cluster reduction with dithionite and apparent reduction potential $E^{\circ\prime}$ (at pH 8, in mV *vs* SHE) determined from potentiometric titrations monitored by low-temperature continuous wave EPR spectroscopy.

NapAB	Apparent reduction half-time rate ($t_{1/2}$ (min))		$E^{\circ\prime}$ (mV *vs* SHE) at pH 8		
	"High *g* resting" Mo(V)	$[4Fe4S]^{1+}$	Hemes		$[4Fe\text{-}4S]^{2+/1+}$
			$E^{\circ\prime}{}_1$	$E^{\circ\prime}{}_2$	
Wild type	15 ± 5[a]	< 1[a] (fast)	25 ± 20	−100 ± 10	−110 ± 10
K56H	20 ± 5	10 ± 3	−40 ± 30	−140 ± 30	−340 ± 10
K56M	50 ± 10	50 ± 10	10 ± 20	−120 ± 30	−520 ± 50
K56M[b]	< 10–15 min	2 ± 1			

[a] From ref [26].
[b] In the presence of methylviologen at a concentration of 5 μM.

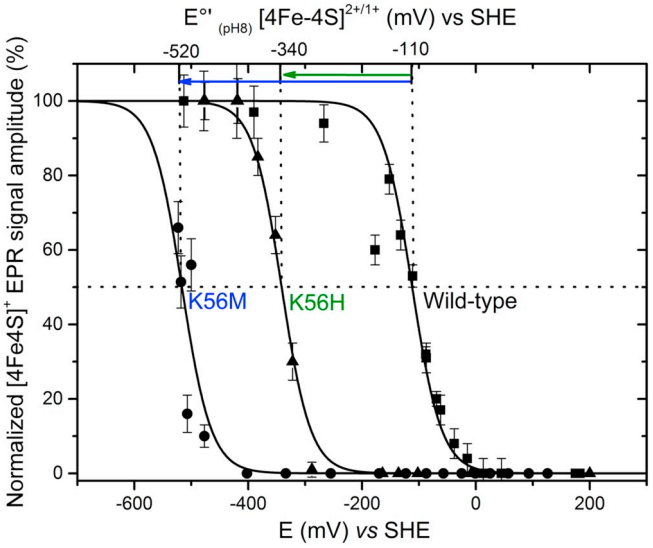

Fig. 7. Redox titrations of the $[4Fe\text{-}4S]^{2+/1+}$ center from the wild-type nitrate reductase NapAB (■), K56H (▲) and K56M (●) mutants from *R. sphaeroides* at pH 8. Potentiometric titrations were performed by reporting the variation of amplitude of the $[4Fe\text{-}4S]^{1+}$ EPR signal as a function of the redox potential measured in the titration cell. Experimental data were fitted using a one-electron Nernst equation. The best parameters determined for the $[4Fe\text{-}4S]^{2+/1+}$ transition were $E^{\circ\prime}{}_{pH8} = -110$ mV ± 10 *vs* SHE for the wild-type NapAB, −340 mV ± 10 *vs* SHE for the K56H mutant and − 520 mV ± 50 *vs* SHE for the K56M mutant. In the case of the K56M mutant, we extrapolated the maximum of amplitude of the $[4Fe\text{-}4S]^{1+}$ signal (that enables to determine the plateau) from the measure of the EPR signal intensity for the most reduced data points.

mutants, namely K56R, K56M and K56H, were designed and produced in *R. sphaeroides*. While K56R did not expressed in *R. sphaeroides*, both K56M and K56H mutants were produced and purified to homogeneity. Enzyme assays revealed that mutation of Lys56 into Met or His strongly affects the turnover number k_{cat} for nitrate reduction by a factor of 10 to 20 at pH 7. Nevertheless, the Michaelis constants K*m* and especially the catalytic efficiency k_{cat}/K*m* (Table 1) found for the mutants and wild-type enzymes indicate that affinity for nitrate as well as catalysis at the active site are not impacted by lysine substitution. Moreover, in the K56H mutant, lowering the pH of the buffered solution to 6 partially restores the enzyme activity to 50% of that of the wild-type enzyme. This roughly correlates to the pKa ~6 for the acid-base transition of the imidazole ring of the histidine which bears a positive charge in its acidic imidazolium form.

In order to understand why the enzyme activity is impacted by the mutation, we performed a comparative and detailed study by EPR spectroscopy of the electronic and structural properties of the redox cofactors of the enzyme. Spin quantitation of the EPR signals confirms the insertion of one [4Fe-4S] center and two hemes per protein in the K56M and K56H NapAB mutants. Moreover, in both mutants, *g*-values of the EPR signals of the hemes and of the [4Fe-4S] center show that their structural properties are globally unaffected. The Mo(V) "high *g*" signal that issues from a resting state of the Mo-cofactor was also observed in all K56H and in some K56M preparations. This observation, together with metal content analysis, indicate that the Mo-cofactor is correctly inserted within the catalytic subunit. The *g*-values and linewidths of the $[4Fe\text{-}4S]^{1+}$ signal suggest little variations of its electronic properties in both mutants, which is consistent with weak perturbation due to mutation of the secondary coordination sphere. This is also supported by the small differences observed in the spin-lattice relaxation properties of the [4Fe-4S] cluster as deduced from microwave power saturation and relaxation broadening studies. In the wild-type NapAB protein, HYSCORE experiments exhibit two weakly-coupled nitrogen nuclei in the vicinity of the [4Fe-4S] cluster likely originating from protein backbone. The nitrogen correlation peaks are not modified by the Lys56 mutation which shows that they do not arise from Lys56. The HYSCORE spectra around the proton Larmor frequency also reveal no significant changes upon Lys mutation that would result from hydrogen-bond disruption. This suggests that the Lys residue is no longer H-bonded in the reduced state of the FeS center. Nevertheless, removal of hydrogen-bond involving amino acids from the secondary coordination sphere could be difficult to probe because: 1) several weakly-coupled ^{1}H-nuclei contribute to the broad spot detected at ^{1}H-Larmor frequency of the 2D-spectra, and/or 2) this hydrogen-bond involves an atom of the cluster on which the spin density is too weak to lead to proton hyperfine coupling detectable by HYSCORE (with the conditions used in these experiments). Finally, our spectroscopic studies indicate that the studied mutations of lysine at this position do not disturb the overall electronic and structural properties of the metal centers.

Kinetics of reduction with dithionite of the [4Fe-4S] center was unusually slow in NapAB mutants with some apparent half-time reduction constants of 10 min and 50 min at pH 8 for K56H and K56M, respectively. By contrast, this reduction was almost instantaneous in the wild-type enzyme (sub-minute timescale) and could not be resolved in the conditions of our experiments. On the contrary, the kinetics of reduction of the hemes in the mutants and wild-type NapAB was apparently kept equal and almost instantaneous. Assuming that the most favorable electron route from dithionite to the [4Fe-4S] center passes through the hemes from NapB, Lys mutation thus impairs the kinetics of the intramolecular electron transfer from the hemes to the [4Fe-4S] cluster. Redox titrations show that mutation of Lysine 56 severely impacts the reduction potential of the [4Fe-4S] cluster while the macroscopic reduction potentials of the hemes are nearly unchanged. To our knowledge, this is one of the most pronounced effect reported on mutation of the secondary coordination sphere of a [4Fe-4S] center [47]. As a matter of fact, the reduction potential of the [4Fe-4S] cluster is lowered by 230 mV in the K56H mutant and by about 400 mV in the K56M mutant at pH 8 with respect to the wild-type enzyme.

Considering the heme redox potentials given in Table 3, the electron transfer step from the hemes to the [4Fe-4S] cluster is therefore much thermodynamically unfavorable (uphill electron transfer) in the K56 mutants.

The influence of these redox potential variations of the [4Fe-4S] cluster on the rate of electron transfer between the hemes and the FeS cluster was estimated with the help of the Marcus equation (Eq. (4)), which describes the kinetics of electron transfer within proteins. In addition to the temperature T, three main parameters determine the kinetic rate constant k_{ET} of electron transfer between redox centers that are the reorganization energy (λ), the electronic coupling factor T_{ab} and the Gibbs free energy variation $\Delta_r G^\circ$ related to the redox potential difference between the two redox centers [48,49]:

$$k_{ET} = \frac{2\pi}{\hbar}\frac{|T_{ab}^2|}{\sqrt{4\pi\lambda k_B T}}\ exp\left(\frac{-(\Delta_r G^\circ + \lambda)^2}{4\lambda k_B T}\right) \quad (4)$$

Reorganization energy (λ) is related to redox-dependent nuclear perturbations such as changes in bond lengths and angles within the inner sphere of the redox centers and changes of the surrounding medium. Electronic coupling factor (T_{ab}) relies on the degree of overlap of the wavefunctions of the reactant and product states (*i.e.* the two redox centers before, and after, electron transfer). T_{ab} strongly depends on the nature of the medium (covalent bonds, hydrogen bonds and vacuum) between both redox centers. Considering 1) that the electronic factor T_{ab} and the reorganization energy λ are unchanged between the wild-type and the mutants and 2) that only the redox potential difference between heme and FeS center varies, the variations of k_{ET} are directly related to the change of $\Delta_r G^\circ$ (Eq. (5)):

$$\ln(k_{ET}) = A - (\Delta_r G^\circ + \lambda)^2/4\ \lambda\ k_B\ T \quad (5)$$

A is a constant parameter. By taking a single mean value for the heme redox potential $E^{\circ\prime}$ of −40 mV (wild-type and K56M) or −90 mV (K56H), and the FeS redox potential value given in Table 3, the $\Delta_r G^\circ$ values (expressed in mV) were found equal to 70 mV, 250 mV and 480 mV at pH 8 for the WT, K56H and K56M, respectively. With a reasonable value of 0.5 eV for λ [50], at the temperature of 298 K, the electron transfer rate k_{ET} is found to decrease by 2 orders of magnitude between the wild-type and the K56H mutant, and by 5 orders of magnitude in the K56M mutant relatively to the wild-type. Catalysis at the active site being unaffected by Lys mutation, the decreased enzyme activity observed in the K56 mutants should result from a high thermodynamic barrier step presented by the [4Fe-4S] cluster. In other words, intramolecular electron transfer from the hemes to the [4Fe-4S] cluster becomes rate-limiting in the catalysis in the K56H and K56M mutants.

Our study hence clearly demonstrates the large influence of K56 on the redox properties of the [4Fe-4S] cluster. Residues from the secondary coordination sphere play important roles in fine-tuning the redox properties of electron-transfer centers in proteins through different interactions such as hydrogen bonding interactions, solvent accessibility or local electrostatic interactions [47,51]. The X-ray structure of the oxidized *Rs*NapAB reveals two putative weak hydrogen-bonds between the side-chain of K56 and the FeS cluster, NH^+_{3Lys56}…S_{Cys54} of 3.9 Å and NH^+_{3Lys56}…bridging sulfur of 4.2 Å (Fig. 1). In the K56M mutant, suppression of the putative positive charge on Lys and hydrogen-bondings to the FeS cluster consistently elicits a decrease of the E° by stabilizing the oxidized state of the [4Fe-4S] cluster [51]. Very interestingly, the decrease of 400 mV reported herein is much larger than the ΔE° reported for mutation within the secondary coordination sphere of FeS clusters. To the best of our knowledge, point mutations of residues from the secondary coordination sphere of FeS clusters usually induce variations of the E° up to 150 mV [52–56]. However, a few studies reported some higher variations of E° which were interpreted, besides the expected effect of the mutation, as a change in solvent accessibility to the FeS cluster [57]. Careful analysis of the two NapAB crystal structures available (from *R. sphaeroides* at a resolution of 3.2 Å [9] and from *Cupriavidus necator* at a resolution of 1.6 Å [11]) reveals that K56 is the only ionizable residue in the second coordination sphere of the [4Fe-4S] cluster. In addition to the two hydrogen-bonds with the side-chain of K56, the [4Fe-4S] cluster can form two hydrogen-bonds with amide side-chain of N49 and N53 and several hydrogen-bonds with amides from the protein backbone. One water molecule is also visible on the high resolution structure of NapAB from *C. necator* and is hydrogen-bonded to the S-Cys22 ligand of the [4Fe-4S] cluster (Fig. SI-6). The water molecule forms a hydrogen-bond network between K56, the FeS cluster and the *P*-pyranopterin of the Mo-cofactor. It should be noticed that this water molecule is also found in crystal structures of NapA and of the closely-related Fdh. Replacement of K56 may result locally in a modification of the hydrogen-bond network around the position 56 and the FeS cluster and a change in the hydration sphere of the FeS cluster. In addition to the removal of positive charge of Lys, these different effects can contribute in the additive manner to cause the noteworthy variation of E° measured in the K56M mutant. This structural rearrangement hypothesis would need to be confirmed by a high resolution crystal structure of the K56M mutant and these works are in progress.

In the K56H mutant, introduction of histidine in place of lysine leads to removal of the positive charge at basic pH (pH 8) but may keep hydrogen bonding to the FeS cluster, depending on orientation of the imidazole ring. First redox titration studies at different pH reveal that the E° of the [4Fe-4S] cluster strongly depends on pH in the K56H mutant at the difference of the wild-type enzyme. Interestingly, the decrease in $\Delta E^\circ_{(FeS,K56H-\ FeS,wt)}$ at pH 6 is of only 50 mV against 230 mV at pH 8. This suggests that the protonation and the positive charge of the imidazole ring of the histidine returns the $E^{\circ\prime}$ of the [4Fe-4S] to a value closer to that of the wild type at pH 6, concomitantly with large recovery of enzyme activity. Further spectroscopic investigations are required to possibly probe hydrogen bonds network around the [4Fe-4S] cluster in the K56H mutant as recently shown in FeS cluster N_2 of respiratory Complex I [58].

The findings of the present study are consistent with former mutagenesis studies on *Ec*NarGHI and *Ec*DmsABC that show that introduction of a polar serine in place of Arg (the counterpart of Lys in NarA and DmsA) provides mutants with slightly decreased quinol oxidase activities [21,22]. Impaired activities were interpreted as an impact of Arg mutation on the intramolecular electron transfer pathway. Moreover, the reduction potential of the [4Fe-4S] center located in the NarG catalytic subunit (called FeS_0) was decreased by 115 mV in the R94S-NarG mutant, concomitantly with a loss of enzyme activity of 70% [22]. The polarity of serine residue as well as its ability to form hydrogen-bonds to the FeS cluster may explain why the effects of the Arg to Ser mutation on redox potential of FeS_0 cluster of Nar are moderated in comparison with those observed in *Rs*NapAB.

To summarize, the present work, together with former studies, clearly show that the existence of a positively-charged (Lys or Arg) residue in the secondary coordination sphere of the FeS cluster (FeS_0), conserved in the catalytic subunit of virtually all the Mo-*bis*PGD enzymes, strongly influences the E° of the cluster through electrostatic interactions and/or hydrogen-bonds. This residue is also certainly an important structural factor for incorporation and stabilization of the FeS cluster within the catalytic subunit, as suggested by the detrimental effect of Lys mutation in K58R and K58Q mutants of *Synechococcus* sp. NarB [25]. Comparison of the $E^{\circ\prime}$ for the [4Fe-4S] center reported in the various Nas and Nap characterized so far reveals that this thermodynamic parameter strongly varies from −15 mV to -250 mV *vs* SHE within the dimeric NapAB enzymes (from *R. sphaeroides*, *E. coli*, *C. necator* and *Paraccocus pantotrophus*) and from +20 to −390 mV for the monomeric (assimilatory and dissimilatory) enzymes (from *R. sphaeroides*, *E. coli*, *D. desulfuricans*, and *Synechococcus elongatus*) [11]. This values was also found strongly dependent on the oligomerization state (NapA *vs* NapAB) in the enzymes from *R. sphaeroides* and *E. coli* [9,10].

This highlights the influence of the overall protein environment in fine-tuning the reduction potential of the [4Fe-4S] center which could then modulate kinetics of intramolecular electron transfer and consequently the overall catalytic activity of the enzyme. This latter aspect also deserves further investigations.

Transparency document

The Transparency document associated with this article can be found, in online version.

Acknowledgements

The authors are grateful to the EPR facilities available at the national EPR network RENARD (IR CNRS 3443) and the Aix-Marseille University EPR center. This work was funded by the CNRS, Aix-Marseille University, the A*Midex foundation of Aix-Marseille University (project MicrobioE, grant number ANR-11-IDEX-0001-02) and the Agence Nationale de la Recherche (MOLYERE project, grant number 16-CE29-0010-01). We thank Maxime Rollo for his help in the analysis of iron-sulfur center relaxation properties and Mathilde Tribout for the last purifications of the K56H mutant.

Appendix A. Supplementary data

Supplementary data to this article can be found online at https://doi.org/10.1016/j.bbabio.2019.01.003.

References

[1] R. Hille, Molybdenum enzymes containing the pyranopterin cofactor: an overview, Metal Ions in Biological Systems, 2002, pp. 187–226.
[2] A. Magalon, P. Ceccaldi, B. Schoepp-Cothenet, The prokaryotic Mo/W-bisPGD enzymes family, Molybdenum and Tungsten Enzymes: Biochemistry, The Royal Society of Chemistry, 2017, pp. 143–191.
[3] S. Grimaldi, B. Schoepp-Cothenet, P. Ceccaldi, B. Guigliarelli, A. Magalon, The prokaryotic Mo/W-bisPGD enzymes family: a catalytic workhorse in bioenergetic, Biochim. Biophys. Acta 8-9 (2013) 1048–1085.
[4] T. Hettmann, R.A. Siddiqui, J. von Langen, C. Frey, M.J. Romao, S. Diekmann, Mutagenesis study on the role of a lysine residue highly conserved in formate dehydrogenases and periplasmic nitrate reductases, Biochem. Biophys. Res. Commun. 310 (2003) 40–47.
[5] J.C. Boyington, V.N. Gladyshev, S.V. Khangulov, T.C. Stadtman, P.D. Sun, Crystal structure of formate dehydrogenase H: catalysis involving Mo, molybdopterin, selenocysteine, and an Fe_4S_4 cluster, Science 275 (1997) 1305–1308.
[6] H. Raaijmakers, S. Macieira, J.M. Dias, S. Teixeira, S. Bursakov, R. Huber, J.J. Moura, I. Moura, M.J. Romao, Gene sequence and the 1.8 A crystal structure of the tungsten-containing formate dehydrogenase from Desulfovibrio gigas, Structure 10 (2002) 1261–1272.
[7] M. Jormakka, S. Tornroth, B. Byrne, S. Iwata, Molecular basis of proton motive force generation: structure of formate dehydrogenase-N, Science 295 (2002) 1863–1868.
[8] J.M. Dias, M.E. Than, A. Humm, R. Huber, G.P. Bourenkov, H.D. Bartunik, S. Bursakov, J. Calvete, J. Caldeira, C. Carneiro, J.J. Moura, I. Moura, M.J. Romao, Crystal structure of the first dissimilatory nitrate reductase at 1.9 A solved by MAD methods, Structure 7 (1999) 65–79.
[9] P. Arnoux, M. Sabaty, J. Alric, B. Frangioni, B. Guigliarelli, J.M. Adriano, D. Pignol, Structural and redox plasticity in the heterodimeric periplasmic nitrate reductase, Nat. Struct. Biol. 10 (2003) 928–934.
[10] B.J. Jepson, S. Mohan, T.A. Clarke, A.J. Gates, J.A. Cole, C.S. Butler, J.N. Butt, A.M. Hemmings, D.J. Richardson, Spectropotentiometric and structural analysis of the periplasmic nitrate reductase from Escherichia coli, J. Biol. Chem. 282 (2007) 6425–6437.
[11] C. Coelho, P.J. Gonzalez, J.G. Moura, I. Moura, J. Trincao, M. Joao Romao, The crystal structure of Cupriavidus necator nitrate reductase in oxidized and partially reduced states, J. Mol. Biol. 408 (2011) 932–948.
[12] D.P. Kloer, C. Hagel, J. Heider, G.E. Schulz, Crystal structure of ethylbenzene dehydrogenase from Aromatoleum aromaticum, Structure 14 (2006) 1377–1388.
[13] M.D. Youngblut, C.L. Tsai, I.C. Clark, H.K. Carlson, A.P. Maglaqui, P.S. Gau-Pan, S.A. Redford, A. Wong, J.A. Tainer, J.D. Coates, Perchlorate reductase is distinguished by active site aromatic gate residues, J. Biol. Chem. 291 (2016) 9190–9202.
[14] G.B. Seiffert, G.M. Ullmann, A. Messerschmidt, B. Schink, P.M. Kroneck, O. Einsle, Structure of the non-redox-active tungsten/$[^4Fe{:}^4S]$ enzyme acetylene hydratase, Proc. Natl. Acad. Sci. U. S. A. 104 (2007) 3073–3077.
[15] M.G. Bertero, R.A. Rothery, M. Palak, C. Hou, D. Lim, F. Blasco, J.H. Weiner, N.C.J. Strynadka, Insights into the respiratory electron transfer pathway from the structure of nitrate reductase A, Nat. Struct. Biol. 10 (2003) 681–687.
[16] M. Jormakka, D. Richardson, B. Byrne, S. Iwata, Architecture of NarGH reveals a structural classification of Mo-bisMGD enzymes, Structure 12 (2004) 95–104.
[17] P.J. Ellis, T. Conrads, R. Hille, P. Kuhn, Crystal structure of the 100 kDa arsenite oxidase from Alcaligenes faecalis in two crystal forms at 1.64 A and 2.03 A, Structure 9 (2001) 125–132.
[18] T.P. Warelow, M. Oke, B. Schoepp-Cothenet, J.U. Dahl, N. Bruselat, G.N. Sivalingam, S. Leimkuhler, K. Thalassinos, U. Kappler, J.H. Naismith, J.M. Santini, The respiratory arsenite oxidase: structure and the role of residues surrounding the rieske cluster, PLoS One 8 (2013) e72535.
[19] M. Jormakka, K. Yokoyama, T. Yano, M. Tamakoshi, S. Akimoto, T. Shimamura, P. Curmi, S. Iwata, Molecular mechanism of energy conservation in polysulfide respiration, Nat. Struct. Mol. Biol. 15 (2008) 730–737.
[20] T. Wagner, U. Ermler, S. Shima, The methanogenic CO_2 reducing-and-fixing enzyme is bifunctional and contains 46[$_4$Fe-$_4$S] clusters, Science 354 (2016) 114–117.
[21] C.A. Trieber, R.A. Rothery, J.H. Weiner, Multiple pathways of electron transfer in dimethyl sulfoxide reductase of Escherichia coli, J. Biol. Chem. 269 (1994) 7103–7109.
[22] R.A. Rothery, M.G. Bertero, T. Spreter, N. Bouromand, N.C. Strynadka, J.H. Weiner, Protein crystallography reveals a role for the FS_0 cluster of Escherichia coli nitrate reductase A (NarGHI) in enzyme maturation, J. Biol. Chem. 285 (2010) 8801–8807.
[23] R.A. Rothery, C.A. Trieber, J.H. Weiner, Interactions between the molybdenum cofactor and iron-sulfur clusters of Escherichia coli dimethylsulfoxide reductase, J. Biol. Chem. 274 (1999) 13002–13009.
[24] R.A. Rothery, G.J. Workun, J.H. Weiner, The prokaryotic complex iron-sulfur molybdoenzyme family, Biochim. Biophys. Acta 1778 (2008) 1897–1929.
[25] A.P. Srivastava, M. Hirasawa, M. Bhalla, J.S. Chung, J.P. Allen, M.K. Johnson, J.N. Tripathy, L.M. Rubio, B. Vaccaro, S. Subramanian, E. Flores, M. Zabet-Moghaddam, K. Stitle, D.B. Knaff, Roles of four conserved basic amino acids in a ferredoxin-dependent cyanobacterial nitrate reductase, Biochemistry 52 (2013) 4343–4353.
[26] J.G. Jacques, V. Fourmond, P. Arnoux, M. Sabaty, E. Etienne, S. Grosse, F. Biaso, P. Bertrand, D. Pignol, C. Leger, B. Guigliarelli, B. Burlat, Reductive activation in periplasmic nitrate reductase involves chemical modifications of the Mo-cofactor beyond the first coordination sphere of the metal ion, Biochim. Biophys. Acta 2 (2014) 277–286.
[27] S. Najmudin, P.J. Gonzalez, J. Trincao, C. Coelho, A. Mukhopadhyay, N.M. Cerqueira, C.C. Romao, I. Moura, J.J. Moura, C.D. Brondino, M.J. Romao, Periplasmic nitrate reductase revisited: a sulfur atom completes the sixth coordination of the catalytic molybdenum, J. Biol. Inorg. Chem. 13 (2008) 737–753.
[28] F. Biaso, B. Burlat, B. Guigliarelli, DFT investigation of the molybdenum cofactor in periplasmic nitrate reductases: structure of the Mo(V) EPR-active species, Inorg. Chem. 51 (2012) 3409–3419.
[29] R.K. Clayton, C. Smith, Rhodopseudomonas spheroides: high catalase and blue-green double mutants, Biochem. Biophys. Res. Commun. 3 (1960) 143–145.
[30] M. Sabaty, C. Avazeri, D. Pignol, A. Vermeglio, Characterization of the reduction of selenate and tellurite by nitrate reductases, Appl. Environ. Microbiol. 67 (2001) 5122–5126.
[31] D. Pignol, J.M. Adriano, J.C. Fontecilla-Camps, M. Sabaty, Crystallization and preliminary X-ray analysis of the periplasmic nitrate reductase (NapA-NapB complex) from Rhodobacter sphaeroides f. sp. denitrificans, Acta Crystallogr. D Biol. Crystallogr. 57 (2001) 1900–1902.
[32] S. Dementin, P. Arnoux, B. Frangioni, S. Grosse, C. Leger, B. Burlat, B. Guigliarelli, M. Sabaty, D. Pignol, Access to the active site of periplasmic nitrate reductase: insights from site-directed mutagenesis and zinc inhibition studies, Biochemistry 46 (2007) 9713–9721.
[33] H. Rupp, K.K. Rao, D.O. Hall, R. Cammack, Electron spin relaxation of iron-Sulphur proteins studied by microwave power saturation, Biochim. Biophys. Acta 537 (1978) 255–260.
[34] P. Bertrand, B. Guigliarelli, J.-P. Gayda, P. Sétif, P. Mathis, An interpretation of the peculiar magnetic properties of center X in photosystem I in terms of a ^2Fe-^2S cluster, Biochim. Biophys. Acta Bioenergetics 933 (1988) 393–397.
[35] J. Caldeira, V. Belle, M. Asso, B. Guigliarelli, I. Moura, J.J.G. Moura, P. Bertrand, Analysis of the electron paramagnetic resonance properties of the $[^2Fe$-$^2S]^{1+}$ centers in molybdenum enzymes of the xanthine oxidase family: assignment of signals I and II, Biochemistry 39 (2000) 2700–2707.
[36] P. Hofer, A. Grupp, H. Nebenfuhr, M. Mehring, Hyperfine sublevel correlation (HYSCORE) spectroscopy - a 2D electron-spin-resonance investigation of the squaric acid radical, Chem. Phys. Lett. 132 (1986) 279–282.
[37] C. More, V. Belle, M. Asso, A. Fournel, G. Roger, B. Guigliarelli, P. Bertrand, EPR spectroscopy: a powerful technique for the structural and functional investigation of metalloproteins, Biospectroscopy 5 (1999) S3–18.
[38] J.P. Gayda, P. Bertrand, C. More, J. Le Gall, R.C. Cammack, Energy of the low-lying excited levels for some reduced [$_4$Fe-$_4$S] ferredoxins, from the relaxation broadening of the E.P.R. Signals, Biochem. Biophys. Res. Commun. 99 (1981) 1265–1270.
[39] C.D. Brondino, M.C. Passeggi, J. Caldeira, M.J. Almendra, M.J. Feio, J.J. Moura, I. Moura, Incorporation of either molybdenum or tungsten into formate dehydrogenase from Desulfovibrio alaskensis NCIMB 13491; EPR assignment of the proximal iron-sulfur cluster to the pterin cofactor in formate dehydrogenases from sulfate-reducing bacteria, J. Biol. Inorg. Chem. 9 (2004) 145–151.
[40] Z. Dermoun, G. De Luca, M. Asso, P. Bertrand, F. Guerlesquin, B. Guigliarelli, The NADP-reducing hydrogenase from Desulfovibrio fructosovorans: functional interaction between the C-terminal region of HndA and the N-terminal region of HndD subunits, Biochim. Biophys. Acta 1556 (2002) 217–225.
[41] H.L. Flanagan, D.J. Singel, Analysis of N-14 ESEEM patterns of randomly oriented

solids, J. Chem. Phys. 87 (1987) 5606–5616.
[42] H.L. Flanagan, D.J. Singel, The impact of excitation-frequency of the nuclear modulation of electron-spin echoes-N-14 hyperfine and quadrupole interactions of DPPH in disordered solids, Chem. Phys. Lett. 137 (1987) 391–397.
[43] S. Grimaldi, R. Arias-Cartin, P. Lanciano, S. Lyubenova, B. Endeward, T.F. Prisner, A. Magalon, B. Guigliarelli, Direct evidence for nitrogen ligation to the high stability semiquinone intermediate in Escherichia coli nitrate reductase A, J. Biol. Chem. 285 (2010) 179–187.
[44] S. Stoll, A. Schweiger, EasySpin, a comprehensive software package for spectral simulation and analysis in EPR, J. Magn. Reson. 178 (2006) 42–55.
[45] C.S. Butler, S.A. Fairhurst, S.J. Ferguson, A.J. Thomson, B.C. Berks, D.J. Richardson, D.J. Lowe, Mo(V) co-ordination in the periplasmic nitrate reductase from Paracoccus pantotrophus probed by electron nuclear double resonance (ENDOR) spectroscopy, Biochem. J. 363 (2002) 817–823.
[46] V. Fourmond, B. Burlat, S. Dementin, P. Arnoux, M. Sabaty, S. Boiry, B. Guigliarelli, P. Bertrand, D. Pignol, C. Leger, Major Mo(V) EPR signature of Rhodobacter sphaeroides periplasmic nitrate reductase arising from a dead-end species that activates upon reduction. Relation to other molybdoenzymes from the DMSO reductase family, J. Phys. Chem. B 112 (2008) 15478–15486.
[47] J. Liu, S. Chakraborty, P. Hosseinzadeh, Y. Yu, S. Tian, I. Petrik, A. Bhagi, Y. Lu, Metalloproteins containing cytochrome, iron-sulfur, or copper redox centers, Chem. Rev. 114 (2014) 4366–4469.
[48] H.R. Williamson, B.A. Dow, V.L. Davidson, Mechanisms for control of biological electron transfer reactions, Bioorg. Chem. 57 (2014) 213–221.
[49] P. Bertrand, Application of electron transfer theories to biological systems, Structure and Bonding, Springer Berlin Heidelberg, Berlin, Heidelberg, 1991, pp. 1–47.
[50] R. Kummerle, J. Gaillard, P. Kyritsis, J.M. Moulis, Intramolecular electron transfer in [$_4$Fe-$_4$S] proteins: estimates of the reorganization energy and electronic coupling in Chromatium vinosum ferredoxin, J. Biol. Inorg. Chem. 6 (2001) 446–451.
[51] P. Hosseinzadeh, Y. Lu, Design and fine-tuning redox potentials of metalloproteins involved in electron transfer in bioenergetics, Biochim. Biophys. Acta 1857 (2016) 557–581.
[52] J.A. Birrell, C. Laurich, E.J. Reijerse, H. Ogata, W. Lubitz, Importance of hydrogen bonding in fine tuning the [^{2}Fe-^{2}S] cluster redox potential of HydC from Thermotoga maritima, Biochemistry 55 (2016) 4344–4355.
[53] P. Kyritsis, R. Kummerle, J.G. Huber, J. Gaillard, B. Guigliarelli, C. Popescu, E. Munck, J.M. Moulis, Unusual NMR, EPR, and Mossbauer properties of Chromatium vinosum 2[$_4$Fe-$_4$S] ferredoxin, Biochemistry 38 (1999) 6335–6345.
[54] E.J. Leggate, J. Hirst, Roles of the disulfide bond and adjacent residues in determining the reduction potentials and stabilities of respiratory-type Rieske clusters, Biochemistry 44 (2005) 7048–7058.
[55] V.W. Cheng, Q.M. Tran, N. Boroumand, R.A. Rothery, E. Maklashina, G. Cecchini, J.H. Weiner, A conserved lysine residue controls iron-sulfur cluster redox chemistry in Escherichia coli fumarate reductase, Biochim. Biophys. Acta 1827 (2013) 1141–1147.
[56] A. Aliverti, W.R. Hagen, G. Zanetti, Direct electrochemistry and EPR spectroscopy of spinach ferredoxin mutants with modified electron transfer properties, FEBS Lett. 368 (1995) 220–224.
[57] J.A. Zuris, D.A. Halim, A.R. Conlan, E.C. Abresch, R. Nechushtai, M.L. Paddock, P.A. Jennings, Engineering the redox potential over a wide range within a new class of FeS proteins, J. Am. Chem. Soc. 132 (2010) 13120–13122.
[58] N. Le Breton, J.J. Wright, A.J.Y. Jones, E. Salvadori, H.R. Bridges, J. Hirst, M.M. Roessler, Using hyperfine electron paramagnetic resonance spectroscopy to define the proton-coupled electron transfer reaction at Fe-S cluster N_2 in respiratory complex I, J. Am. Chem. Soc. 139 (2017) 16319–16326.